PCCP

Accepted Manuscript

ROYAL SOCIETY OF CHEMISTRY

www.rsc.org/pccp

PCCP

ARTICLE

Synthesis of Functional xLayMn/KIT-6 and Feature of Hot Coal Gas Desulphurization

Hong Xia, Fengmei Zhang, Zhaofei Zhang and Bingsi Liu*

To enhance the stability of sorbent during continuous desulphurization-regeneration cycles, KIT-6 with 3D pore channels was used as support for sorbents. A series of mesoporous xLayMn/KIT-6 sorbents with different La/Mn atomic ratios were fabricated by a sol-gel method and their desulphurization properties in hot coal gas were investigated at 700-850 ^{o}C. 3La97Mn/KIT-6 performed the best at 800 ^{o}C with breakthrough sulphur capacity of 11.56 g sulfur/100 g sorbent. The eight successive desulphurization (800 ^{o}C)-regeneration (600 ^{o}C) cycles revealed that 3La97Mn/ KIT-6 with endurable regeneration ability could obtain 80% of initial sulphur capacity. It indicated better desulphurization performance compared to pure 3La97Mn and 3La97Mn/MCM-41. The fresh and used xLayMn/KIT-6 sorbents were characterized by means of BET, XRD, HRTEM, XPS and H_2-TPR techniques. The XRD patterns and HRTEM images of fresh and used 3La97Mn/KIT-6 verified that the utilization of KIT-6 suppressed effectively the aggregation of Mn_2O_3 particles and improved the stability of sorbent.

1 Introduction

Due to the fact that more than 70% energy consumption relies on coal resources in China, the air pollution is induced which can be attributed to the by-product of fly ash, compounds of containing nitrogen and sulphur during the coal combustion. According to the report[1], China had overtaken other nations in the worldwide as the largest emitter of SO_2 since 2005, which should be mainly attributed to the coal-derived power station. Therefore, a system named integrated gasification-combined cycle (IGCC) was developed to replace the traditional coal-derived power station to realize a high effective usage of coal resources and lower emission of contaminant. Furthermore, the H_2S in coal-derived gas not only corrupt the pipeline or gas turbine and poison the catalysts (*e.g* Fischer-Tropsch synthesis[2]) for downstream process, but also can be a source of acid rain which threats the environment and the human health. In the meantime, environmental legislations have been presented to limit the sulphur content in fossil-derived gas. So it is necessary to keep the emission of H_2S below 100 ppmv in IGCC unit. Conventional gas-cleaning techniques at low temperature, such as amine scrubbers[3] and wet limestone[4] desulphurization, have been applied to remove the H_2S in the coal gas, which are disadvantageous in energy saving due to the huge heat loss during gas cooling and reheating stage. Therefore, the desulphurization for hot coal gas is needed to improve the overall thermal efficiency from an energy saving point of view.

Recently, there are comprehensive reports concerning copper[5-10], zinc[11-14], manganese[7, 10, 12, 15-20], ferric, calcium[4, 21, 22] and rare earth element[23-26] used as based sorbents of hot coal gas desulphurization. According to the report of Westmoreland[27, 28], MnO was stable in strong reducing environment and possessed promising potential for hot coal gas desulphurization in the temperature range of 400-1000 ^{o}C, which is superior to V_2O_3, CaO and ZnO due to high initial sulphidation rate. Although MnO has a relative lower desulphurization precision compared with zinc and ferric oxides, its high desulphurization efficiency with endurable regeneration ability and high sulphur capacity at 800-1000 ^{o}C have attracted considerable attention of researchers[16, 17, 29]. When copper, zinc, ferric, rare earth elements oxides were doped to Mn-based sorbents, the thermodynamic equilibrium efficiency reacted with H_2S can increase remarkably. As report of Flytzani-Stephanopoulos[26], Ce and La oxides were stable at higher than 800 ^{o}C and the ultra deep removal of H_2S could be achieved.

Pure metal oxides as desulphurizers are confronted with the serious scientific problems, such as diffusion resistance, mechanical strength and sintering during hot coal gas desulfurization. Recently, many inert materials were used as support of metal oxides, such as TiO_2, ZrO_2, Al_2O_3 and mesoporous MCM-41 and SBA-15. However, the utilization of the active particles was low due to low surface area and character of microporous or 1D channel of the support. In the meantime, the macroporous material, such as cordierite, indeed suffered from the pulverization and low utilization of sorbent because of the low surface area. Thus, there is significant interest to use novel support, such as MCM-48 or KIT-6. However, KIT-6 presented a superior performance in resistance to pore blockage due to its unique pore structure with three dimensional channels, which have been applied in adsorption of CO_2. In this study, the mesoporous silica KIT-6 with high surface area and large pore volume was synthesized using as the support of sorbents and this design could take advantage of unique pore structure of KIT-6 to improve the gas diffusion in reaction as well as the stability of the sorbent. A series of xLayMn/KIT-6 sorbents were prepared by a sol-gel method and their desulphurization activities were investigated on a quartz reactor. The properties of fresh and used sorbents were characterized by the means of BET, XRD, HR-TEM, XPS, FT-IR and H_2-TPR techniques.

2Experimental section

2.1 Synthesis of KIT-6 and xLayMn/KIT-6 Sorbents

Mesoporous KIT-6 was prepared according to the report of Kleitz et al[30], *i.e.* 9 g of pluronic P123 was dissolved in 325 g of deionized water (DW) and 17.4 g of HCl (37%) under vigorous stirring to form a clear and transparent solution. Subsequently, 9 g of butanol was added with stirring at 35 °C for 1 h. After 19.35 g of TEOS was added drop-wise to the aforementioned clear solution, this mixture was continuously stirred at 35 °C for another 24 h and then was transferred into a Teflon-lined stainless steel autoclave for hydrothermal synthesis at 100 ^{o}C for 24 h under static condition. After cooled down it to room temperature (RT), the white precipitate was filtered and dried at 100 ^{o}C for 24 h. Finally, the white powder was calcined in air at 550 ^{o}C for 6 h.

A series of xLayMn/KIT-6 sorbents with different La/Mn atomic ratios were prepared by means of a sol-gel method according to the report of Zhang *et al*[31]. 0.32 g of $La(NO_3)_3{\bullet}6H_2O$ was dissolved in 25 mL DW and 8.52 g of 50wt% $Mn(NO_3)_2$ solution, followed by addition of 5 mL HNO_3 (6 mol/L). After the addition of 7.74 g of citric acid, 2 g of as-prepared KIT-6 support was added to the aforementioned solution. The mixture was kept at 60 ^{o}C until it became a viscous yellow gel and then aged at RT for two days. Finally, the gel was dried at 60 ^{o}C and calcined at 550 ^{o}C for 6 h to obtain dark brown 50wt%3La97Mn/KIT-6. A series of 50wt% xLayMn/KIT-6 sorbents were fabricated according to same procedure as 3La97Mn/KIT-6, which were denoted as 10La90Mn/ KIT-6, 5La95Mn/KIT-6, 3La97Mn/KIT-6 and 100Mn/KIT-6, the numbers before La and Mn stood for the molar number in mixed metal oxides, respectively. The loadings of active metal oxides (La_2O_3 and Mn_2O_3) for all samples was 50 wt%.

2.2 Characterization of Sorbents

Nitrogen adsorption isotherms of KIT-6, fresh and used 50wt% xLayMn/KIT-6 sorbents were obtained at 77 K on a domestic adsorption system[32]. Prior to the analysis, the samples were degassed at 200 ^{o}C for 2 h. BET surface area, pore volume and average pore diameter were calculated based on adsorption isotherm while pore size distribution was estimated by BJH (Barrett, Joyner & Halenda) method.

The small-angle X-ray diffraction (XRD) patterns of KIT-6, fresh and used sorbents were recorded with a Rigaku D/max 2500 v/pc automatic diffractometer equipped with Ni filtered Cu K_α radiation (20 kV, 30 mA). Wide-angle XRD patterns were measured with a PANalytical automatic diffractometer using Ni-filtered Cu Kα radiation (λ = 0.15406 nm) at settings of 40 kV and 50 mA. The cell parameters of all samples were calculated by the following equation: $a_0 = \sqrt{6} \times d(211)$. The pore wall thickness was estimated by the formula h = a_0/3.0919- D/2[33], D is the mesopore size calculated based on BJH method. The fine structures of fresh and used sorbents were investigated by HRTEM on a JEM-2100F electron microscopy operated at 200 kV. FT-IR spectra of fresh and regenerated 3La97Mn/KIT-6 at 600, 700 and 800 ^{o}C were collected on BIO-RAD FTS 3000 spectrophotometer.

The temperature-programmed reduction (TPR) experiments were performed using a TPR-2910 Micromeritics (USA) instrument, equipped with a thermal conductivity detector (TCD). 0.1995 g of samples was pretreated at 200 ^{o}C in argon (30 mL/min) for 60 min. After cooling to 60 ^{o}C in argon atmosphere, TPR profiles were taken from 60 to 900 ^{o}C (10 ^{o}C/min) in 10% H_2/Ar mixed gas (30 mL/min) and the signals of hydrogen consumption were recorded using TCD.

The X-ray photoelectron spectroscopy (XPS) signals were obtained with a PHI-1600 ESCA spectrometer equipped with Al Kα X-ray source (1486.6 eV). The binding energies (BEs) of the sample were calibrated with the contaminant C 1s line (284.6 eV).

2.3Desulfurization and Regeneration Tests for Sorbents

The desulfurization performance of the sorbents for hot coal gas was investigated over a fixed-bed quartz tubular micro-reactor. The experimental setup was described in details elsewhere[34]. The inlet stream was controlled by mass flow controllers (D07-7B/ZM, Beijing Sevenstar Electronics Co., Ltd., China) at 180 mL/min. Typically, 0.5 g sorbent was packed into the reactor (i.d. 10 mm) and the reaction temperature was controlled by a K-type thermal-couple. The sorbents were first heated to the reaction temperature in N_2 at the rate of 10 ^{o}C/min and the simulated hot coal gas with composite of 66.44% N_2, 13.84% H_2, 19.36% CO and 0.36% H_2S was then introduced to the reactor for desulfurization. The concentration of H_2S in inlet and outlet gas was analyzed by iodometric titration method to obtain breakthrough curve of H_2S and breakthrough sulphur capacity (the outlet H_2S concentration of lower than 50 ppmv is defined as the breakthrough point). The performance of sorbents was evaluated by the breakthrough sulphur capacity (BSC) according to equation (1):

$$SC\left(\frac{g\ of\ sulfur}{100\ g\ of\ sorbent}\right) = WHSV \times \frac{M_S}{V_m} \times \left[\int_0^t \left(C_{in} - C_{out}\right) dt\right] \times 10^{-4} \tag{1}$$

Where SC represents the effective sulphur capacity (g•S/100 g sorbents); $WHSV$ is weight hour space velocity (L/(h•g)); M is molecular weight of sulphur (g/mol); V_m is the molar volume of H_2S at standard pressure and 25 ^{o}C (24.5 L/mol); C_{in} and C_{out} are the inlet and outlet concentration (ppmv) of H_2S, respectively; t is the breakthrough time for desulphurization (h). The effective utilization of sorbent can be defined as the ratio of BSC with the theoretical sulphur capacity (TSC).

The regeneration temperature was optimized in the range of 600～800 ^{o}C over aforementioned reactor. The used sorbent was first heated to appointed temperature in N_2 (77 mL/min) at a rate of 10 ^{o}C/min and then regenerated in 5% O_2/N_2 mixture (100 mL/min) until the concentration of SO_2 in exit could not be detected by $KMnO_4$ solution as a indicator. The regenerated samples were treated in the N_2 atmosphere for 1 h to keep the residual metal sulphate decomposing.

3 Results and discussion

3.1 BET Analysis

To investigate the variation in structure of sorbents during the desulphurization and regeneration, the nitrogen adsorption isotherms and pore size distributions of KIT-6, fresh and used sorbents were shown in Fig. 1. It could be seen that KIT-6 exhibited type-IV curve defined by International Union of Pure and Applied Chemistry (IUPAC), which was characteristic of mesoporous materials. A sharp capillary condensation step in the range of p/p_0 = 0.7-0.9 (Fig. 1A) and a narrow pore size distribution (D_p) at approximately 10.6 nm (Fig. 1D) were observed, an indicative of the uniform large channels existed within KIT-6. As shown in Fig. 1B, the nitrogen adsorption isotherms of fresh sorbents did not vary remarkably, which indicated that the introduction of metal oxides did not destroy the characteristic of mesoporous KIT-6. However, compared with KIT-6, there was a decline in height of adsorption mutation (Fig. 1B-C) and the pore size distribution after the metal oxide was incorporated into KIT-6 or the sorbents used in hot coal gas desulphurization (Fig. 1E-F).

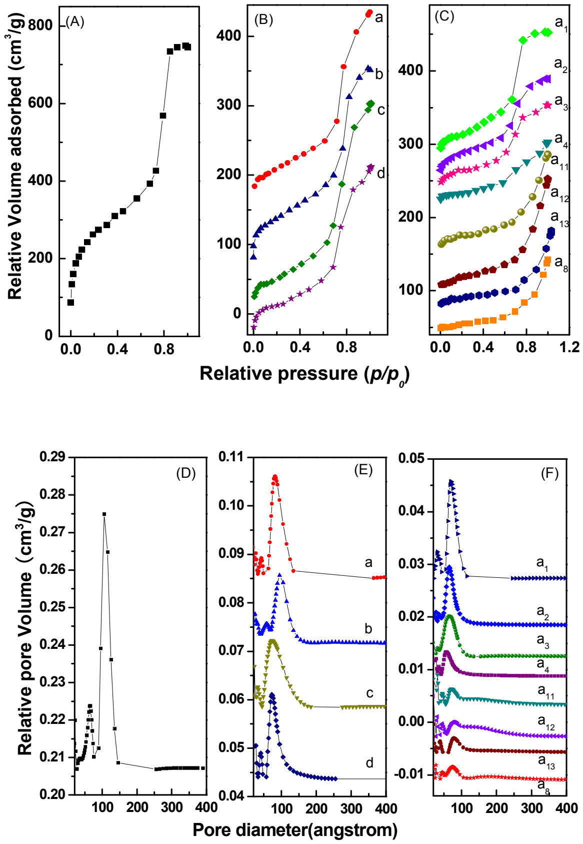

Fig. 1 N_2 adsorption isotherms (A-C)and pore size distribution(D-F) of KIT-6 and fresh (a) 3La97Mn/KIT-6, (b) 5La95Mn/KIT-6, (c) 10La90Mn/KIT-6, and (d) 100Mn/KIT-6; (a_1-a_4) 3La97Mn/KIT-6 used at 700, 750, 800, 850 °C, respectively; (a_{11}-a_{13}) 3La97Mn/KIT-6 regenerated at 600, 700 and 800 °C after third cycles; (a_8) 3La97Mn/KIT-6 regenerated at 600 °C after eighth cycles.

Table 1. Total pore volume (V_t), Mesopore volume (V_{meso}), Micropore volume (V_m), Average pore diameter (D_a) and BET surface area (S_{BET}) of KIT-6, fresh and used xLayMn/KIT-6

Sample	V_t (mm³/g)	V_{meso} (mm³/g)	V_m (mm³/g)	D_a (nm)	S_{BET} (m²/g)
KIT-6	1093	762	331	2.33	938
La3Mn97/KIT-6	381	309	72	3.56	214
La5Mn95/KIT-6	395	308	87	3.11	254
La10Mn90/KIT-6	414	344	70	4.04	205
Mn100/KIT-6	336	262	74	3.57	188
S-700-La3Mn97/KIT-6	254	201	53	3.51	145
S-750-La3Mn97/KIT-6	197	148	49	2.64	149
S-800-La3Mn97/KIT-6	163	126	37	3.05	107
S-850-La3Mn97/KIT-6	113	86	27	1.66	68
S-800-La5Mn95/KIT-6	177	137	40	2.71	131
S-800-La10Mn90/KIT-6	117	93	24	4.03	58
S-800-Mn100/KIT-6	224	180	44	3.23	139
R-S-3-600-La3Mn97/KIT-6	162	132	30	4	81
R-S-3-700-La3Mn97/KIT-6	176	158	18	4.35	81
R-S-3-800-La3Mn97/KIT-6	100	83	17	3.57	56
R-S-8-600-La3Mn97/KIT-6	111	99	12	4.93	45

Notes: The physical parameters of all samples were calculated by BJH method.

As listed in Table 1, S_{BET} and V_t of KIT-6 were 938 m^2/g and 1.093 cm^3/g, respectively. Both S_{BET} and V_t of fresh sorbents decreased to 188-254 m^2/g and 0.336-0.414 cm^3/g, respectively due to the loadings of metal oxides in mesoporous channels of KIT-6. For used sorbents, after desulphurized at 700-850 °C, there was a drastic decline in both S_{BET} and V_t due to the replacement of metal oxides by metal sulphides with large molecular sizes (Table 1). Moreover, the S_{BET} and V_t of used sorbents decreased with the increment of desulphurization temperature. According to the report of Zhang *et al.*[35], the increment of calcination temperature on mesoporous silica can enhance the polymerization degree of $\equiv$Si-O-Si$\equiv$ bonds but with smaller pore diameter and lower surface area. After the 3La97Mn/KIT-6 underwent 8th desulphurization-regeneration cycles, approximately 30% of S_{BET} and V_t was still maintained, indicated the stability of mesoporous structure in sorbent, which was favourable to the diffusion of gas and heat in mesoporous channels of sorbents.

3.2 XRD Analysis

Small-angle powder X-ray diffraction (XRD) patterns of KIT-6, fresh and used sorbents were shown in Fig. 2. The small angle XRD patterns of KIT-6 have three diffraction peaks at 2θ = 0.97, 1.1, 1.76°, which was ascribed as the reflections of (211), (220), (332)

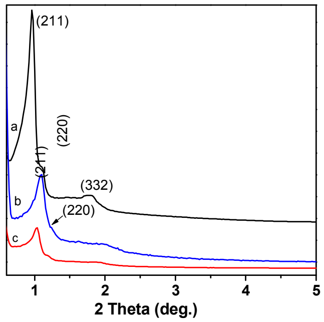

Fig. 2 Small-angle XRD patterns of (a) KIT-6, (b) fresh and use (c) 3La97Mn/KIT-6.

planes in the discontinuous cubic Ia3d space group, respectively. As shown in Fig. 2b, the XRD patterns of fresh 3La97Mn/KIT-6 verified that the mesoporous cubic structure of KIT-6 was not destroyed after the loading of metal oxides. However, the reduction in intensity of XRD peaks could be attributed to a decrease in the electron density contrast upon the introduction of metal oxides into the mesoporous channels of KIT-6, and this behaviour was identical with the nitrogen adsorption results (Fig. 1B and 1E). The wall thickness (2.72 nm) can be calculated from the relationship (h = a_0/3.0919- D_p/2) of the unit cell parameter, a_0 (20.79 nm) with the most probable diameter D_p (8.2 nm), based on the interplanar spacing, d ($n\lambda = 2d\sin\theta$) estimated from the peak corresponding to (211) reflections in 3La97Mn/KIT-6, which was higher than that (2.1 nm) of KIT-6. This revealed that the enhancement of the pore wall thickness was due to the loading of metal oxides, resulting in better thermal stability. For 3La97Mn/KIT-6 after desulphurization at 800 °C, the pore wall thickness was 3.2 nm, which was attributed to the metal sulphides with large molecular size (r (S^{2-}) = 184 pm, r (Mn^{2+}) = 80 pm) substitution for metal oxides with small molecular size (r(O^{2-}) = 140 pm, r (Mn^{3+}) = 66 pm) on pore wall of mesoporous channels. However, the sharp peak at 2θ = 1.09° indicated that the bicontinuous mesoporous network of sorbent was still preserved after desulphurization (Fig. 2c).

The textural features of fresh, used and regenerated sorbents were investigated by wide-angel XRD. As shown in Fig. 3, there was no signal of silicates, which indicated that no reaction occurred between metal oxides and supports. For all fresh sorbents, the manganese oxides existed mainly in the form of Mn_2O_3 [PDF#65-7467] and Mn_3O_4 [PDF#18-0803] phases. For 100Mn/KIT-6, the peaks at 23.14 °, 32.95 °, 38.23 °, 45.17 °, 49.35 ° and 55.18 ° were assigned to Mn_2O_3 phase [PDF#65-7467], while there were only weak peaks of Mn_3O_4 [PDF#18-0803] at 2θ = 18.02 ° and 36.04 °. However, the diffraction peaks of Mn_2O_3 became weak and widen (Fig. 3 A(b-d)) accompanied with transition from Mn_2O_3 to Mn_3O_4 with the increment of La_2O_3 loading. The ionic radius of doped La^{3+} is between those of Mn^{3+} (0.066 nm) and O^{2-} (0.140 nm). Therefore, the La^{3+} ions (0.102 nm) can replace the Mn^{3+} sites, which further vary the close-packed of particles and increase the defects in the crystal structure.[36] In the meantime, MnO_x crystallite sizes reduced after the doping with La_2O_3 due to segregation of the doped La^{3+} ions at the grain boundary, which inhibited the aggregation of grains.[37] However, there was no La diffraction peak to be observed up to 10 wt% La loading. This indicated that La_2O_3 presented in an amorphous state or very fine particles without the detection using of X-ray diffractometer.[38]The particles of MnO_x and La_2O_3 lowered remarkably and were dispersed highly on the support as a result of the synergetic effects which will result in the variation of sorbent in the structural properties.[39, 40]

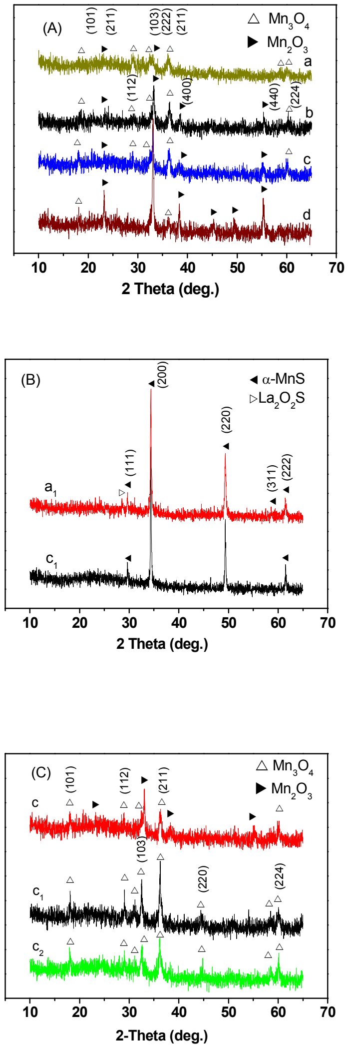

Fig. 3 Wide-angle XRD patterns of (A) fresh and (B) sulphided (a, a_1) 10La90Mn/KIT-6, (b) flesh5La95Mn/KIT-6, (c, c_1) fresh and sulphided 3La97Mn/KIT-6, (d) flesh 100Mn/KIT-6 and; (C) fresh and regenerated(c, c_1, c_2) 3La97Mn/KIT-6 after third cycles and eighth cycles, respectively.

For used 10La90Mn/KIT-6, the peaks of La_2O_2S at 2θ = 28.51° and α-MnS [PDF#65-0891](2θ = 29.62°, 34.34°, 49.35°, 61.50°) were observed in XRD patterns. However, there was only α-MnS [PDF#65-0891] phase to be detected in used 3La97Mn/KIT-6(Fig. 3B(c_1)) due to the low content of La species.

As for XRD patterns of 3La97Mn/KIT-6 regenerated at 600 °C for 3 and 8 times, respectively (Fig. 3C), there was a significant variation in structure compared to fresh 3La97Mn/KIT-6 without the formation of sulphate. The peaks at 2θ = 18.02°, 28.97°, 32.41°, 36.04°, 44.37°, 58.76° and 60.02° were assigned to Mn_3O_4 [PDF#18-0803], indicating that Mn_3O_4 was the most stable spinel phase in regenerated sorbents, plausibly due to low oxygen atmosphere(6% v O_2/N_2 mixture). However, there is no obvious change in intensity and width of the XRD peaks of 3La97Mn/KIT-6 regenerated at 800 °C for 3rd and 8th cycles. In a word, the metal oxides can disperse again on the inner surface of KIT-6 during the regeneration treatments (Fig. 3C(c_1,c_2)), which was favourable to the multi-utilization of sorbent.

3.3 HRTEM Images of Sorbents

The fine structures of KIT-6, fresh, used and regenerated 3La97Mn/KIT-6 were investigated by means of HRTEM technique. As shown in Fig. 4a-b, the HRTEM images and corresponding FT diffraction patterns (inset of Fig. 4a-b) revealed that KIT-6 exhibited clear lattice fringes. The distance between two dark strips is about 7～8 nm, close to the results (8～9.1 nm) calculated by small-angle XRD ($n\lambda = 2d\sin\theta$), an indicative of the highly ordered 3D pore structures[41]. The HRTEM images of fresh 3La97Mn/KIT-6 illustrated that KIT-6 still remained the double gyroidal mesoporous structure and the active species of metal oxides were dispersed uniformly in the channel of KIT-6 after metal oxides, Mn_2O_3 and La_2O_3 loadings (Fig. 4c). It can be seen from the result of EDX analysis that Mn and La oxides were incorporated successfully with KIT-6 support. Small part of metal oxides were aggregated on the outer surface of KIT-6 and formed metal oxide particles with the diameter of 10-14 nm due to higher oxide loadings (50%)(Fig. 4e). As shown in Fig. 4e, the magnification HRTEM image of metal oxide crystallites revealed the existence of regular crystalline particles and the two *d*-spacing obtained by the distance between light-dark strips were 0.27 and 0.48 nm, corresponding to the (222) plane of cubic Mn_2O_3 and the (101) plane of Mn_3O_4 (JCPDS 18-0803), respectively. Fig. 4f showed the selected area electron diffraction (SAED) in this region. The light dots dispersed highly on diffusion concentric circles indicated that metal oxides existed mainly in polycrystalline particles with small amount of nanocrystallites. The crystal *d*-spacings estimated via SAED patterns were 0.25 and 0.16 nm, corresponding to the (222) and (440) plane of Mn_2O_3 nanoparticles. Therefore, the phase analysis of fresh 3La97Mn/KIT-6 sorbent verified that active species existed in Mn_2O_3 and Mn_3O_4 mixed crystallites, similar to the results of XRD analysis (Fig. 3A(c)). Besides, there is no signal of La_2O_3 in SAED images, plausible duo to the loadings of trace La_2O_3.

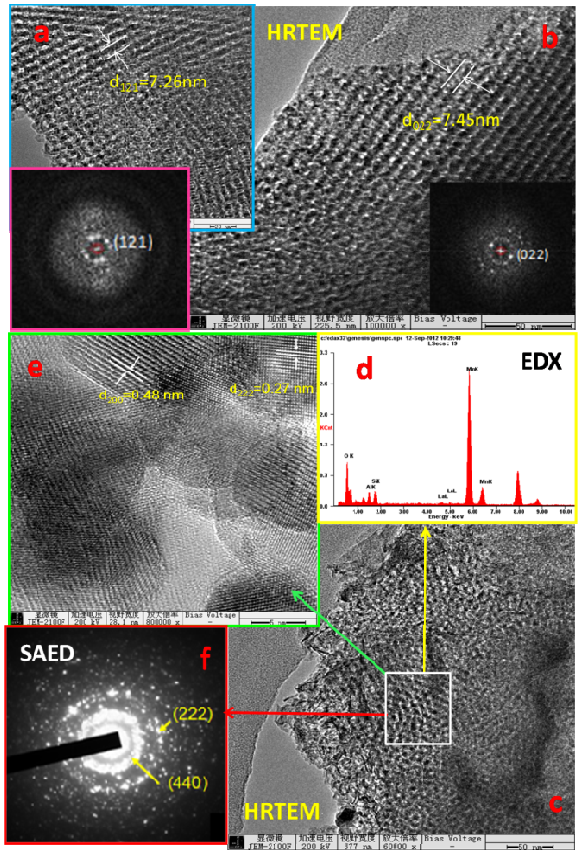

Fig. 4 HRTEM images of KIT-6, viewed from (a) [111], (b) [311] phase directions (inset: FT diffraction patterns); (c) HRTEM image (d)corresponding EDX analysis of fresh 3La97Mn/KIT-6; (e) HRTEM image (f) SAED patterns of MnO*x* species of fresh 3La97Mn/KIT-6.

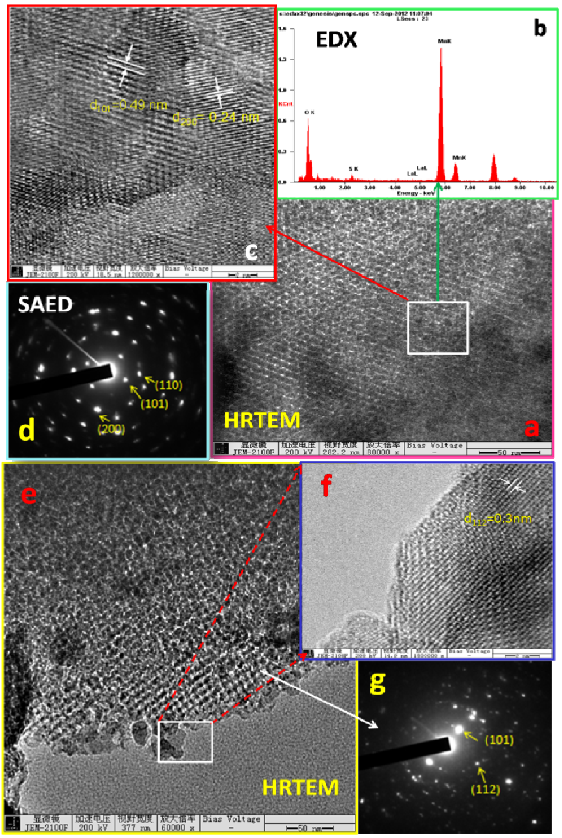

Fig. 5 (a) HRTEM image and (b, d) corresponding EDX analysis and SAED patterns of 3La97Mn/KIT-6 after sulphidation at 800 °C; (c) HRTEM image of

sulphides of 3La97Mn/KIT-6 after sulphidation at 800 ^{o}C; (e)HRTEM images of 3La97Mn/KIT-6 after regeneration, (f) HRTEM images and (g) the corresponding to SAED patterns of regenerated metal oxides in 3La97Mn/KIT-6.

HRTEM image and EDX analysis of 3La97Mn/KIT-6 after sulphidation at 800 ^{o}C illustrated that the mesoporous silica KIT-6 framework still remained intact, indicating a hydrothermal stability of the support. Furthermore, there were no significant aggregations of metal sulphides to appear, indicating that the utilization of KIT-6 was effective to depress the aggregation of metal particles insides channels (Fig. 5a). SAED image revealed that the diffraction characteristics of polycrystallites reduced and the properties of crystals intensified remarkably. In the meantime, the symmetrical array of diffraction dots appeared. The crystal *d*-spacing calculated by diffraction dots in SAED image were 0.27 and 0.33 nm, corresponding to the (200) and (111) planes of cubic MnS crystallites, respectively, similar to the distance (0.24 nm) between two dark strips in magnification HRTEM image of MnS crystallites. Besides, we observed strong diffraction dots with the *d*-spacing of 0.49 nm on SAED pattern, attributed to the (101) planes of Mn_3O_4 (JCPDS 18-0803) that did not react in 3La97Mn/KIT-6 sorbent although Mn_3O_4 species were not detected in XRD patterns. In the meantime, the *d*-spacing (0.49 nm) of the (101) planes of Mn_3O_4 was observed in magnification HRTEM image (Fig. 5c). In a word, the crystallites of MnS grew up and aggregated to a certain extent after sulphidation reaction compared to fresh 3La97Mn/KIT-6.

Fig. 5e-g presented the TEM/SAED analysis for 3La97Mn/KIT-6 regenerated for three cycles. Fig. 5e showed well-reserved 3D mesoporous framework of KIT-6, which facilitated the gas-solid reaction in sorbent through continuous desulphurization-regeneration cycles. The HRTEM image of regenerated particles was observed with *d*-spacing at 0.30 nm (Fig. 5f). The corresponding SAED patterns of active particles indicated that they contributed to (101) and (112) plane of Mn_3O_4, respectively.

3.4 H_2-TPR Measurements

As shown in Fig. 6, there are two minor reduction peaks in the range of 374-436 ^{o}C and a strong peak centred at 567 ^{o}C in H_2-TPR profile of 3La97Mn/KIT-6. The former was ascribed to the reduction of partial Mn oxides on the surface of sorbent, and the latter was attributed to the reduction of Mn_3O_4 and Mn_2O_3 to MnO[42,43] according to the equation[44], $3Mn_2O_3 + H_2 = 2Mn_3O_4 + H_2O$, $Mn_3O_4 + H_2 = 3MnO + H_2O$. On the contrary, the H_2-TPR peaks over 10La90Mn/KIT-6 shifted to low temperature region due to segregation action of La_2O_3 species and two reduction peaks centred at 546 and 750 ^{o}C were ascribed to the reduction of Mn oxides to the MnO[42, 43] and reduction of partial MnO to Mn^0 [45]. This suggested that Mn oxides were reduced more easily with increasing amounts of La_2O_3 species, indicating that the active sites to react with H_2 enhanced due to the smaller sizes and better dispersion of the particles. In addition, the H_2 consumption over 3La97Mn/KIT-6 was higher than that over 10La90Mn/KIT-6, because the former existed mainly in Mn_2O_3 and the latter in Mn_3O_4 species (Fig. 3A), resulting in different H_2-consumption contents between two sorbents.

3.5 XPS Analysis

Fig. 7 showed the XPS spectra of Mn over fresh, used and regenerated 3La97Mn/KIT-6 sorbents. The binding energies (BEs) at 653.6 eV and 641.6 eV can be described to Mn $2p_{1/2}$ and Mn $2p_{3/2}$ in Mn_2O_3 (Fig. 7A(a)). As shown in Fig.7A, there was nearly no difference between Mn 2p peaks before and after desulphurization, i.e. it is difficult to identify the oxidation states of Mn.[46] According to report of Töpfer et al, [47] there was appreciable distinction in Mn3p peaks between Mn^{3+} (49.5 eV) and Mn^{2+} (48.2 eV) ions. Therefore, the spectra of Mn3p were collected in order to verify the chemical states of manganese. The broadening of the Mn3p peak in Fig.7B revealed the different valence states of Mn in fresh 3La97Mn/KIT-6 sorbent, which had been verified by XRD analysis. After smoothing and background subtraction by a fitting of the Mn3p spectrum, there was approximately equal peak area of Mn^{3+}/Mn^{2+}, indicating the coexistence of both Mn^{3+} and Mn^{2+} ions. Fig. 7C showed that MnO_x

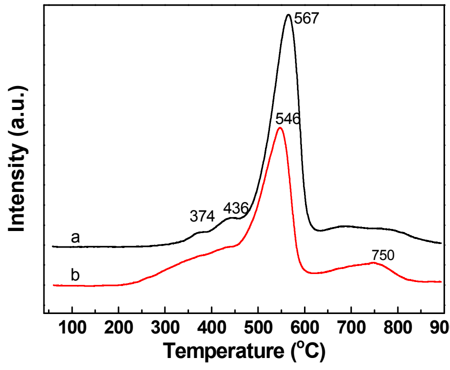

Fig. 6 TPR profiles of (a) 3La97Mn/KIT-6 and (b) 10La90Mn/KIT-6

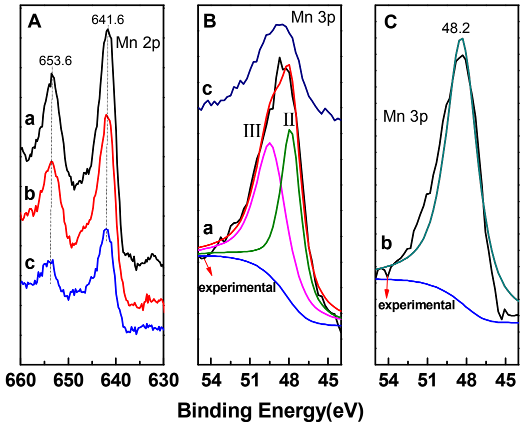

Fig. 7 Mn 2p (A) and Mn 3p (B-C) spectra of fresh (a), used (b) and regenerated (c) 3La97Mn/KIT-6 sorbents.

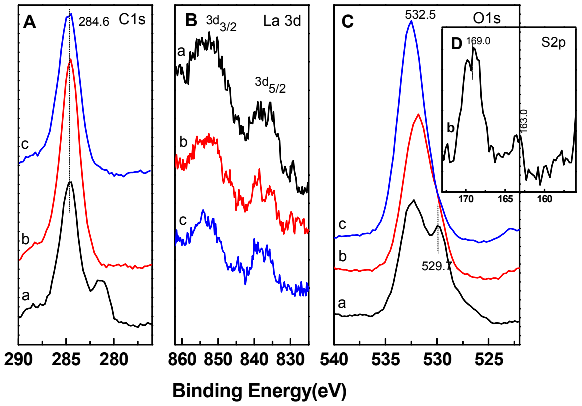

Fig. 8 C 1s (A), La 3d (B), O 1s (C) and S 2p (D) spectra of fresh (a), used (b) and regenerated (c) 3La97Mn/KIT-6 sorbents

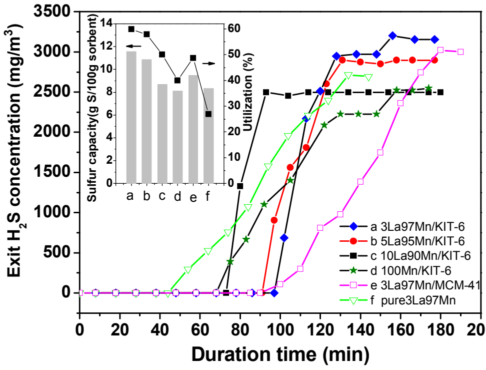

Fig. 9 H_2S breakthrough curves for xLayMn/KIT-6 sorbents with different La/Mn ratios. (a) 3La97Mn/KIT-6, (b) 5La95Mn/KIT-6, (c) 10La90Mn/KIT-6, (d) 100Mn/KIT-6, (e) 3La97Mn/MCM-41 and (f) pure 3La97Mn. Reaction temperature: 800 °C; WHSV=21600 mL/(h•g); feed composition: 66.44% N_2, 13.84% H_2, 19.36% CO, 0.36% H_2S.

was transformed into MnS after desulphurization with the BE values of 48.2 eV. After regeneration, MnS was transformed into Mn_3O_4 (Fig. 7B(c)), which was consistent with XRD results (Fig. 3).

C1s peaks (284.6 eV) in Fig.8A originated from the contaminant carbon species and a shoulder peak at 281.2 eV in C 1s XPS spectra of fresh 3La1097Mn/KIT-6 (Fig. 8A(a)) correlated closely with the formation of carbides. This may stem from incomplete combustion of citric acid during the calcination of sorbent. The La3d$_{5/2}$ BE is 835.5 eV, 16.8 eV apart from the La3d$_{3/2}$ peak (Fig. 8B) in accord with that reported in literature.[48] It could be seen that there was no obvious variation between BEs of La 3d$_{5/2}$ and La 3d$_{3/2}$ before and after sulphidation, meaning that valence states of La remained constant. The peaks at 532.5 eV and 529.7 eV for fresh 3La97Mn/KIT-6 (Fig. 8C) were assigned to O 1s spectra in SiO_2 and metal oxides, respectively. After sulphidation, the O 1s peak at 529.7 eV disappeared (Fig. 8C(b)) and the signal of S 2p at 163.0 eV occurred due to the transformation of metal oxides to metal sulphides (Fig. 8D). The peak at 169.0 eV was attributed to the signal of sulphate. The interaction of sulphides with the oxygen atoms on sorbent will result in the formation of sulphate.

3.6 Effect of La/Mn Atomic Ratios on Performance of Sorbents

The effect of different La/Mn atomic ratios on desulphurization performance of sorbents was shown in Fig. 9. It was worthwhile to note that 100Mn/KIT-6 showed the lowest sulphur capacity (8 g sulphur/100 g sorbent) with slowly deactivation rate (Fig. 9d). The gas-solid reaction between H_2S and MeO$_x$ occurred first on the surface and then extended to the bulk phase. The low sulphur capacity was attributed to the high diffusion resistance of H_2S from surface to bulk due to the aggregation of Mn_2O_3 particles in the absence of La_2O_3 (Fig. 3A(d)). The doping of a small amount of La_2O_3 in the Mn-based sorbent could decrease significantly the particle size and improve the dispersion of Mn species, which can expose more active sites and is favourable to the diffusion of H_2S within active particles. The desulphurization performance might be controlled by the number of the active centres and related to the amount of manganese oxide species having different surface vacancies. However, the sulphur capacity of La_2O_3 itself is low and the reaction rate with H_2S was slow. Therefore, the H_2S breakthrough sulphur capacity (BSC) over 3La97Mn/KIT-6, 5La95Mn/KIT-6 and 10La90Mn/KIT-6 decreased with incremental La_2O_3 loadings. 3La97Mn/KIT-6 exhibited the highest sulphur capacity (11.56 g sulphur/100 g sorbents) with the utilization of about 60%. On the other hand, the XRD patterns of the sorbents also illustrated that Mn_2O_3 transformed gradually into Mn_3O_4 phase with the increase of La_2O_3 species. Ko et al[49] reported that the desulphurization performance of the Mn_2O_3 was better than that of Mn_3O_4 due to the reduction of Mn_2O_3 during sulphur adsorption. The terrace occurrence in desulphurization curve of 10La90Mn/KIT-6 sorbent may originate from the catalytic action of La_2O_2S species to make decomposition of H_2S at high temperature, similar to the catalytic phenomenon of Sm_2O_3S[50]. In addition, 3La97Mn/KIT-6 sorbent exhibited higher breakthrough sulphur capacity when compared with pure 3La97Mn and 3La97Mn/MCM-41. A poor desulphurization performance of the pure 3La97Mn sorbent (0.25 g) at 800 °C was due to the low surface area and pore volume (Table S1 and Fig. S1, Supplementary Information). The low deactivation rate (Fig. 9f) over pure 3La97Mn after breakthrough point meant that there was strong mass transfer limitation when H_2S contacted with MnO*x* in bulk due to the presence of larger Mn_2O_3 particles, which was verified by XRD result (Fig. S2, Supplementary Information). Hence, the utilization of pure 3La97Mn sorbent decreased seriously. In the meantime, the desulphurization performance over 3La97Mn/MCM-41 with straight 1-D pore structure reduced slightly (Fig. 9e) due to both dispersion of Mn_2O_3 particle over the framework and the diffusion resistance of H_2S molecules. The XRD result of 3La97Mn/MCM-41 (Fig. S2(b)) also verified the existence of large active species of Mn_2O_3. In a word, KIT-6 with 3D double gyroidal channel was outstanding candidate for hot coal gas desulphurization due to its special textural properties.

3.7 Effect of Desulphurization Temperature on Performance of 3La97Mn/KIT-6

The effect of desulphurization temperature on the performance for hot coal gas desulphurization was investigated in the range of 700-

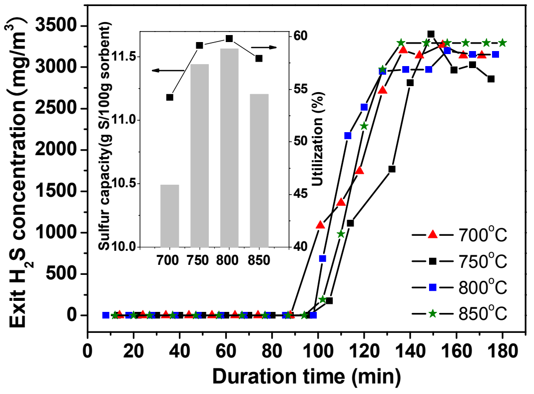

Fig. 10 H_2S breakthrough curves for 3La97Mn/KIT-6 sorbents at different sulphurization temperatures. WHSV=21600mL/(h•g); feed composition: 66.44% N_2, 13.84% H_2, 19.36% CO, 0.36% H_2S.

850 °C. As shown in Fig. 10, the breakthrough time and the corresponding sulphur uptake capacity over 3La97Mn/KIT-6 increased from 700 to 800 °C. According to the report of Bakker *et al*[51], the initial desulphurization reaction rate increased with the increasing reaction temperature. However, the desulphurization performance over 3La97Mn/KIT-6 declined slightly at 850 °C, plausible due to the serious deterioration of mesoporous silica framework. The S_{BET} (68 m^2/g) and V_{meso} (86 mm^3/g) of 3La97Mn /KIT-6 after desulphurized at 850 °C declined significantly (Table 1), which resulted in the rise of H_2S diffusion resistance during the reactions. However, the HRTEM and BET results revealed that the double gyroidal mesoporous structure of 3La97Mn/KIT-6 remained intact (Fig. 5a). As a result, 800 °C was determined as the most feasible temperature.

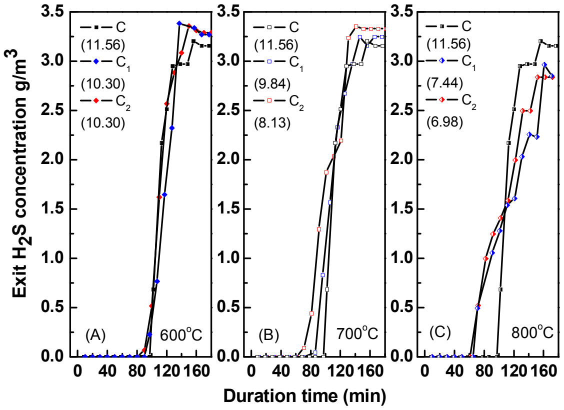

Fig. 11 H_2S breakthrough curves over (C) fresh and (C_1, C_2) regenerated 3La97Mn/KIT-6 sorbents. Desulphurization: 800 °C; WHSV=21600mL/(h•g); feed composition: 66.44% N_2, 13.84% H_2, 19.36% CO, 0.36% H_2S. Regeneration: (A) 600 °C, (B) 700 °C; (C) 800 °C ; WHSV = 7200 mL/(h•g); feed composition: 5% O_2/N_2. The data in parentheses in the upper left is the corresponding sulphur capacity (S/100g sorbent)

3.8 Effect of Regeneration Temperature on Properties of 3La97Mn/KIT-6

The effect of regeneration temperature on the properties of 3La97Mn/KIT-6 was shown in Fig. 11. During desulphurization (800 °C)-regeneration cycles based on the following equation: $3MnS+5O_2=Mn_3O_4+3SO_2 (\Delta H=-3298KJ/mol)$. It can be seen that the regeneration reaction is exothermic, so it should be carried out at temperature as low as possible to avoid the sintering of the sorbents. The H_2S breakthrough curves over 3La97Mn/KIT-6 regenerated at 600 °C almost kept unchangeable and about 89% of initial activity could be remained for 3rd cyclic regeneration (Fig. 11A). In the meantime, HRTEM images and S_{BET} of 3La97Mn/KIT-6 regenerated at this temperature verified the existence of mesoporous structure of 3La97Mn/KIT-6. However, the desulphurization performance of sorbents regenerated at 700 and 800 °C declined, especially at 800 °C. The breakthrough curve became smooth after breakthrough time point (Fig. 11C), because high temperature could induce the collapse of the mesoporous silica framework of sorbent, resulting in the decrease of S_{BET} and V_t (56 m^2/g and 0.10 cm^3/g) (Table 1). Besides, the FT-IR spectra (Fig. 12) of sorbents regenerated at 600-800 °C revealed that the bands (400-700 cm^{-1}) ascribed to the asymmetry, blending and stretching vibration of Mn-O bonds in Mn_2O_3 and Mn_3O_4[52,53] did not vary significantly and the formation of little sulphates increased slightly with incremental regeneration temperature (the bands at 947 cm^{-1} were attributed to the adsorption of SO_4^{2-} [54]). The bands at 1075 and 807 cm^{-1} were ascribed to the asymmetric and symmetric stretching vibration of Si-O[55] for 3La97Mn/KIT-6, which was shifted to 1100 cm^{-1} after regeneration due to the contract in the mean bond length[56-58] of Si-O-Mn in supported metal oxides during transformation from Mn_2O_3 to Mn_3O_4 (Fig. 3C(c_1,c_2)).

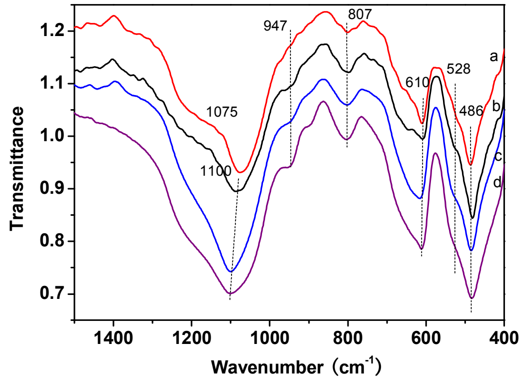

Fig. 12 FT-IR spectras of fresh and regenerated sorbents. (a) fresh 3La97Mn/KIT-6, (b) 3La97Mn/KIT-6 regenerated at 600 °C for 3 cycles,(c) 3La97Mn/KIT-6 regenerated at 700 °C after 3 cycles, (d) 3La97Mn/KIT-6 regenerated at 800 °C after 3 cycles.

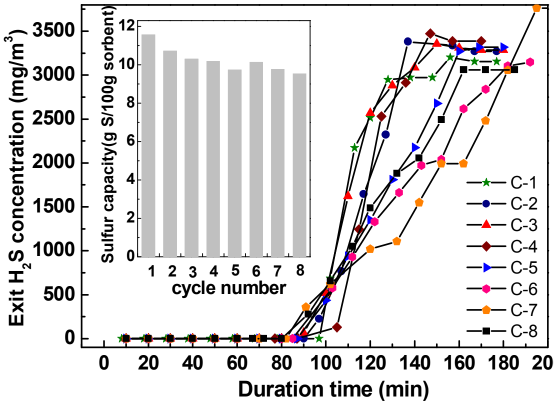

Fig. 13 H_2S breakthrough curves for eighth desulphurization-regeneration cycles over 3La97Mn/KIT-6 sorbent (Inset is corresponding breakthrough sulfur capacity). Desulphurization: T-800 °C; WHSV=21600 mL/(h•g); feed composition: 66.44% N_2, 13.84% H_2, 19.36% CO, 0.36% H_2S. Regeneration: T-600 °C; WHSV= 7200 mL/(h•g); feed composition: 5% O_2/N_2.

3.9 Successive Sulphurization-Regeneration Performance of 3La97Mn/KIT-6

In order to study the regeneration stability, mechanical strength and desulphurization performance of 3La97Mn/KIT-6 sorbents, eight desulphurization-regeneration cycle results and the corresponding sulphur uptake capacity were shown in Fig. 13. It can be seen that the BSC over fresh 3La97Mn/KIT-6 was 11.56 g sulphur /100 g sorbents, which was significantly higher than that over 50%wt $LaFeO_3$/MCM-41 (5.58 g sulphur /100 g sorbents)[59] and the latter was used only at 500-550 °C. This indicated that the addition of Mn active species and the utilization of high stable mesoporous KIT-6 with double gyroidal structure (Scheme 1) increased remarkably the sulphur capacity of sorbent and improved the sulphidation performance at high temperature (800 °C). As shown in scheme 1, the 3D double gyroidal channel of KIT-6 constrained effectively the sintering of active La-Mn species as well as the pulverization of sorbents. Therefore, the performance of the sorbent after 9th cycle was highly stable with ca. 80% of the initial activity. The XRD results of 3La97Mn/KIT-6 verified that the active La-Mn clusters still were dispersed highly on KIT-6 after 3rd and 8th regeneration cycles. The HRTEM images illustrated that mesoporous structure of KIT-6 remained intact (Fig. 5e-f) after successive desulphurization-regeneration.

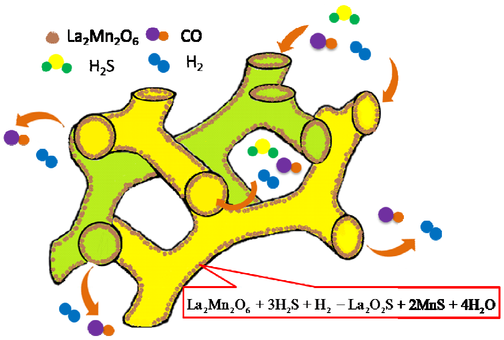

Scheme 1. Scheme of stable xLayMn/KIT-6 with double gyroidal structure for hot coal gas desulphurization.

Conclusions

A series of xLayMn/KIT-6 were prepared by a sol-gel method. The 8th desulphurization-regeneration tests of 3La97Mn/KIT-6 indicated that 3La97Mn/KIT-6 performed well with stable regeneration ability. BET analysis, small-angle XRD and HRTEM images suggested that the mesoporous framework of 3La97Mn/KIT-6 was stable during cyclic regeneration tests. The utilization of KIT-6 ensured the highly dispersion of active particles and confined the migration of active particles during desulphurization-regeneration tests, which was essential for the regeneration of 3La97Mn/KIT-6.

Acknowledgements

We gratefully acknowledge the joint financial support of National Natural Science Foundation of China and BAOSTEEL Group Corporation (Grant 50876122).

References

1 S. Su, B. Li, S. Cui and S. Tao, *Environ. Sci. Technol.* 2011, **45**, 8403-8410.
2 K. Okabe, K. Murata, M. Nakanishi, T. Ogi, M. Nurunnabi and Y. Liu, *Catal. Lett.*, 2009, **128**, 171-176.
3 J. Yan, J. Bao, Z. Jiang, Y. Huang and X. Shen, *Proceedings of the CSEE* , 2009, **29**, 21-26.
4 R. Álvarez-Rodríguez and C. Clemente-Jul, *Fuel*, 2008, **87**, 3513-3521.
5 S. Yasyerli, G. Dogu, I. Ar and T. Dogu, *Ind. Eng. Chem. Res.* 2001, **40**, 5206-5214.
6 Z. Li and M. Flytzani-Stephanopoulos, *Ind. Eng. Chem. Res.* 1997, **36**, 187-196.
7 L. Alonso, J. M. Palacios, E. García and R. Moliner, *Fuel Process. Technol.* 2000, **62**, 31-44.
8 O. Karvan and H. Atakül, *Fuel Process. Technol.* 2008, **89**, 908-915.
9 Z. Ozaydin, S. Yasyerli and G. Dogu, *Ind. Eng. Chem. Res.* 2008, **47**, 1035-1042.
10 E. García, J.M. Palacios, L. Alonso and R. Moliner, *Energy Fuels* 2000, **14** ,1296-1303.
11 X. Bu, Y. Ying, X. Ji, C. Zhang and W. Peng, *Fuel Process. Technol.* 2007, **88**, 143-147.
12 T.-H. Ko, H. Chu and Y.-J. Liou, *J. Hazard. Mater.* 2007, **147**, 334-341.
13 S. Lew, A. F. Sarofim and M. Flytzani-Stephanopoulos, *Ind. Eng. Chem. Res.* 1992, **31** ,1890-1899.
14 E. Sasaoka, S. Hirano, S. Kasaoka, and Y. Sakata, *Energy Fuels*, 1994, **8**, 763-769.
15 P. Dhage, A. Samokhvalov, D. Repala, E. C. Duin, B. J. Tatarchuk, *Phys. Chem. Chem. Phys.*, 2011, **13**, 2179-2187.

16 R. Ben-Slimane and M. T. Hepworth, *Energy Fuels*, 1994, **8**, 1184-1191.

17 R. Ben-Slimane and M. T. Hepworth, *Energy Fuels*, 1995, **9**, 372-378.

18 D. Karayilan, T. Dogu, S. Yasyerli and G. Dogu, *Ind. Eng. Chem. Res.*, 2005, **44**, 5221-5226.

19 R. B. Slimane and J. Abbasian, *Adv. Environ. Res*., 2000, **4**, 147-162.

20 S. Yasyerli, *Process Intensification.*, 2008, **47**, 577-584.

21 L. A. Fenouil and S. Lynn, *Ind. Eng. Chem. Res.*, 1995, **34**, 2334-2342.

22 T. T. Akiti, K. P. Constant, L. K. Doraiswamy, T. D. Wheelock, *Ind. Eng. Chem. Res*. 2002 ,**41**, 587-597.

23 S. Cheah, Y. O. Parent, W. S. Jablonski, T. Vinzant, J. L. Olstad, *Fuel*, 2012, **97**, 612-620.

24 Z. Wang, M. Flytzani-Stephanopoulos, *Energy Fuels* 2005, **19**, 2089-2097.

25 I. Valsamakis, R. Si, M. Flytzani-Stephanopoulos, *J. Power Sources*, 2010, **195**, 2815-2822.

26 M. Flytzani-Stephanopoulos, M. Sakbodin, Z. Wang, *Science*, 2006, **312**, 1508-1510.

27 P. R. Westmoreland, J. B. Gibson, D. P. Harrison, *Environ. Sci. Technol.* 1977, **11**, 488-491.

28 P. R. Westmoreland, D. P. Harrison, *Environ. Sci. Technol.,* 1976, **10** , 659-661.

29 R. Ben-Slimane, M. T. Hepworth, *Energy Fuels* 1994, **8**, 1175-1183.

30 F. Kleitz, S. Hei Choi, R. Ryoo, *Chem. Commun.* 2003, 2136-2137.

31 F. M. Zhang, B. S. Liu, Y. Zhang, Y. H. Guo, Z. Y. Wan, F. Subhan, *J. Hazard. Mater.* 2012, **233-234**, 219-227.

32 B. S. Liu, Y. Zhang, J. F. Liu, M. Tian, F. M. Zhang, C. T. Au, A. S. C. Cheung, *J. Phys. Chem. C,* 2011, **115**, 16954-16962.

33 Y. Q. Dou, Y. Zhai, F. Zeng, X.-X. Liu, B. Tu, D. Zhao, *J. Colloid Interface Sci.* 2010, **341**, 353-358.

34 B. S. Liu, X. N. Wei, Y. P. Zhan, R. Z. Chang, F. Subhan, C. T. Au, *Appl. Catal. B*, 2011,**102**, 27-36.

35 F. Zhang, H. Yan, Y. Yang, M.Yan, C. Yu, B. Tu, D. Zhao, *J. Phys. Chem. B*, 2005, **109**, 8723-8732.

36 R. Xue, J. Yan, Y. Tian, B. Yi, *Acta Phys.-Chim. Sin.*, 2011, **27**, 2340-2347.

37 X. Z. Ding, X. H. Liu, *J. Mater. Res.,* 1998, *13*, 2556.

38 H. Zhao, D. Zhang, F. Wang, T. Wu, J. Gao, *Process Saf. Environ. Prot.*, 2008, **86**, 448-454.

39 H. Zhao, D. Zhang, F. Wang, T. Wu, J. Gao, *Process Saf. Environ. Prot.*, 2009, **87**, 274-280.

40 C. P. Sibu, S. R. Kumar, P. Mukundan, K. G. K. Warrier, *Chem. Mater*, 2002, **14**, 2876-288.

41 K. Soni, B. S. Rana, A. K. Sinha, A. Bhaumik, M. Nandi, M. Kumar, G. M. Dhar, *Appl. Catal. B*, 2009, **90**, 55-63.

42 F. Arena, T. Torre, C. Raimondo, *Phys. Chem. Chem. Phys*. 2001, **3**, 1911-1917.

43 W. Gac, *Appl. Catal. B*, 2007, **75**, 107-117.

44 X. Tang, J. Li, L. Sun, J. Hao, *Appl. Catal. B*, 2010, **99**, 156-162.

45 J. Zhu, D. Xiao, J. Li, X. Yang, *Catal. Lett.*, 2009, **129**, 240-246.

46 T.Y. Li, S.J. Chiang, B.J. Liaw, Y.Z. Chen, *Appl. Catal. B. Environ.* 2011, **103**, 143-148.

47 J. Töpfer, A. Feltz, D. Gräf, B. Hackl, L. Raupach, P. Weissbrodt, *Phys. Stat. Sol.*, 1992, **134**, 405-415.

48 C.D. Wagner, W.M. Riggs, L.E. Davis, J. Moulder, in: G.E. Muilenberg (Ed.), 1st ed., Perkin Elmer Corporation (Physical Electronics), 1979.

49 T.-H. Ko, H. Chu, L.-K, *Chemosphere*, 2005, **58**, 467-474.

50 B. S. Liu, Z. Y. Wan, F. Wang, Y. P. Zhan, M. Tian, A. S. C. Cheung, *J. Hazard. Mater.*, 2014, **267**, 229- 237.

51 W. J. W. Bakker, F. Kapteijn, J. A. Moulijn, *Chem. Eng. J*. 2003, **96**, 223-235.

52 B. Tian, X. Liu, L. A. Solovyov, Z. Liu, H. Yang, Z. Zhang, S. Xie, F. Zhang, B. Tu, C. Yu, O. Terasaki, D. Zhao, *J. Am. Chem. Soc.* 2003, **126**, 865-875.

53 C. M. Julien, M. Massot, C. Poinsignon, *Spectrochimica Acta Part A: Mol. Biomolecular Spectros.* 2004, **60**, 689-700.

54 S. M. Reddy, S. S. Rao, N. Venkanna, *Int. J. Chem. Anal. Sci.* 2011, **2**, 126-129.

55 F. Subhan, B. S. Liu, Y. Zhang, X. G. Li, *Fuel Process. Technol.* 2012, **97**, 71-78.

56 M. Selvaraj, B. H. Kim, T. G. Lee, *Chem. Lett.* 2005, **34**, 1290-1291.

57 M. Selvaraj, P. K. Sinha, K. Lee, I. Ahn, A. Pandurangan, T. G. Lee, *Micropor. Mesopor. Mater.* 2005, **78**, 139-149.

58 S. H. Park, B. H. Kim, M. Selvaraj, T. G. Lee, *J. Ind. Eng. Chem.*, 2007, **13**, 637-643.

59 Z. Y. Wan, B. S. Liu, F. M. Zhang, X. H. Zhao, *Chem. Eng. J.* 2011, **171**, 594-602.